









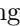


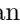



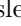




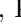






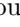

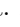




A. Vinokurova , V. S. Vismaya , L. Vitale , V. Vobbilisetti , R. Volpe , B. Wach , M. Wakai , S. Wallner ,  
 E. Wang , M.-Z. Wang , X. L. Wang , Z. Wang , A. Warburton , S. Watanuki , C. Wessel , E. Won ,  
 X. P. Xu , B. D. Yabsley , S. Yamada , W. Yan , S. B. Yang , J. Yelton , J. H. Yin , K. Yoshihara ,  
 C. Z. Yuan , Y. Yusa , B. Zhang , V. Zhilich , Q. D. Zhou , X. Y. Zhou , V. I. Zhukova , and R. Žlebčák   
 (The Belle II Collaboration)

We present GFlaT, a new algorithm that uses a graph-neural-network to determine the flavor of neutral  $B$  mesons produced in  $\Upsilon(4S)$  decays. It improves previous algorithms by using the information from all charged final-state particles and the relations between them. We evaluate its performance using  $B$  decays to flavor-specific hadronic final states reconstructed in a  $362 \text{ fb}^{-1}$  sample of electron-positron collisions collected at the  $\Upsilon(4S)$  resonance with the Belle II detector at the SuperKEKB collider. We achieve an effective tagging efficiency of  $(37.40 \pm 0.43 \pm 0.36)\%$ , where the first uncertainty is statistical and the second systematic, which is 18% better than the previous Belle II algorithm. Demonstrating the algorithm, we use  $B^0 \rightarrow J/\psi K_S^0$  decays to measure the mixing-induced and direct  $CP$  violation parameters,  $S = (0.724 \pm 0.035 \pm 0.014)$  and  $C = (-0.035 \pm 0.026 \pm 0.013)$ .

PACS numbers:

## I. INTRODUCTION

In the standard model,  $CP$  violation arises from an irreducible complex phase in the Cabibbo-Kobayashi-Maskawa (CKM) matrix [1]. Measurements of mixing-induced  $CP$  violation in  $B^0$  meson decays constrain the values of the CKM-unitarity-triangle angles  $\phi_1$  and  $\phi_2$ ,<sup>1</sup> helping us probe for sources of  $CP$  violation beyond the standard model. For example, we learn  $\phi_1$  from  $B^0 \rightarrow J/\psi K^0$  [2–4] and  $\phi_2$  from  $B^0 \rightarrow (\pi\pi)^0$  [5–7],  $(\rho\rho)^0$  [8–10]. These measurements require knowledge of the neutral  $B$  meson flavor. At  $B$  factory experiments,  $B^0$  and  $\bar{B}^0$  mesons are produced in pairs from  $e^+e^-$  collisions at the  $\Upsilon(4S)$  resonance. Since their states are entangled, tagging the flavor of one of the mesons,  $B_{\text{tag}}$ , at the time of its decay determines the flavor of the other one,  $B_{\text{sig}}$ , at the same time [11, 12].

The Belle II [13] experiment reported results using a flavor tagger [14–16] based on algorithms developed by the Belle and BABAR experiments [2, 17]. It uses the kinematic, topology, particle-identification, and charge information of charged final-state particles in the  $B_{\text{tag}}$  decay to infer if they originated from categories of flavor-specific decays. For instance, a charged particle is assigned as being a  $\mu^+$  in a  $B^0 \rightarrow D\mu^+\nu_\mu X$  decay or a  $K^+$  in the subsequent  $D \rightarrow K^+Y$  decay, the charge of which correlates to the  $B_{\text{tag}}$  flavor. This category-based flavor tagger selects the most probable assignment in each category, discards all other possibilities in that category, and then combines the probabilities of the selected assignments to predict the  $B_{\text{tag}}$  flavor.

In this paper, we present a new algorithm, the graph-neural-network flavor tagger, GFlaT, which uses a dynamic-graph-convolutional-neural-network [18] to combine the information from all charged final-state par-

ticles. It improves flavor tagging by accounting for the discarded information in the category-based flavor tagger and correlations between information from final-state particles.

To demonstrate GFlaT, we measure the  $CP$  parameters of  $B^0 \rightarrow J/\psi K_S^0$  from which we calculate  $\phi_1$ . The probability density to observe  $B_{\text{sig}}$  decay at a time  $\Delta t$  from when  $B_{\text{tag}}$  decays with flavor  $q_{\text{tag}}$  (1 for  $B^0$ ,  $-1$  for  $\bar{B}^0$ ) is

$$P(\Delta t, q_{\text{tag}}) = \frac{e^{-|\Delta t|/\tau}}{4\tau} \left\{ 1 + q_{\text{tag}}(1 - 2w)[S \sin(\Delta m_d \Delta t) - C \cos(\Delta m_d \Delta t)] \right\}, \quad (1)$$

where  $q_{\text{tag}}$  is determined by the flavor tagger,  $w$  is the probability to wrongly determine it,  $\tau$  is the  $B^0$  lifetime, and  $\Delta m_d$  is the difference of masses of the  $B^0$  mass eigenstates.<sup>2</sup> Here  $S$  and  $C$ , the parameters of interest, quantify mixing-induced and direct  $CP$  violation, respectively. In the standard model,  $S = \sin 2\phi_1$  and  $C = 0$  to good precision [19–21]. At  $B$  factories, the  $B$  mesons are boosted and have significant momentum in the lab frame, so  $\Delta t$  is determined from the relative displacement of their decay vertices.

To measure  $CP$  parameters in tagged  $B^0$  decays, we must know  $w$ . We determine it from events with the flavor-specific  $B_{\text{sig}}$  decaying as  $B^0 \rightarrow D^{(*)-}\pi^+$ , for which

$$P(\Delta t, q_{\text{sig}}, q_{\text{tag}}) = \frac{e^{-|\Delta t|/\tau}}{4\tau} \left\{ 1 - q_{\text{sig}}q_{\text{tag}}(1 - 2w) \cos(\Delta m_d \Delta t) \right\}, \quad (2)$$

where  $q_{\text{sig}}$  equals the charge of the pion from the  $B_{\text{sig}}$  decay, neglecting the  $\mathcal{O}(10^{-4})$  wrong-sign contribution

<sup>1</sup> These angles are also known as  $\beta$  and  $\alpha$ .

<sup>2</sup> We use a system of units in which  $\hbar = c = 1$  and mass and frequency have the same dimension.

from  $B^0 \rightarrow D^{(*)+}\pi^-$  [22–24]; we implicitly include charge conjugated decays here and throughout. Here we assume  $w$  is independent of the  $B_{\text{sig}}$  decay mode. Flavor taggers also determine the quality of their flavor assignments by the dilution factor,  $r \in [0, 1]$  which approximates  $1 - 2w$ . We determine  $w$  in seven contiguous disjoint intervals ( $r$  bins) defined by the edges  $[0.0, 0.1, 0.25, 0.45, 0.6, 0.725, 0.875, 1.0]$ , as in Ref. [15], and calculate the effective tagging efficiency,

$$\varepsilon_{\text{tag}} = \sum_i \varepsilon_i (1 - 2w_i)^2, \quad (3)$$

where  $\varepsilon_i$  is the average of the efficiencies to tag  $B^0$  and  $\bar{B}^0$  in  $r$  bin  $i$ . An increase in  $\varepsilon_{\text{tag}}$  improves statistical precision for parameters measured in tagged  $B^0$  decays, for example, the statistical uncertainties on  $S$  and  $C$  are proportional to  $1/\sqrt{\varepsilon_{\text{tag}}}$ . The effective tagging efficiency is thus a convenient metric for evaluating tagger performance.

We reconstruct the flavor-specific  $B^0 \rightarrow D^{(*)-}\pi^+$  decays from  $D^- \rightarrow K^+\pi^-\pi^-$  and  $D^{*-} \rightarrow \bar{D}^0\pi^-$  with  $\bar{D}^0 \rightarrow K^+\pi^-$ ,  $K^+\pi^-\pi^0$ , or  $K^+\pi^-\pi^+\pi^-$ . We fit the background-subtracted  $\Delta t$  distributions to extract flavor tagger parameters, including  $w$ , and determine the  $\Delta t$  resolution model.

For the measurements of  $S$  and  $C$ , we reconstruct the  $B_{\text{sig}}$  candidates by combining  $K_S^0 \rightarrow \pi^+\pi^-$  with  $J/\psi \rightarrow e^+e^-$  or  $\mu^+\mu^-$ . The values of  $S$  and  $C$  are extracted via a fit to the background-subtracted  $\Delta t$  distribution using the flavor tagger parameters and  $\Delta t$  resolution model determined from the study of  $B^0 \rightarrow D^{(*)-}\pi^+$ .

This paper is organized as follows. We first discuss the Belle II detector and the simulation software used in the study in Sec. II. Section III describes the GFlaT algorithm, including input variables, training procedure, and a discussion on the improvement from the category-based flavor tagger. Section IV presents the evaluation of GFlaT's performance using the flavor-specific process,  $B^0 \rightarrow D^{(*)-}\pi^+$ . We describe the measurement of  $S$  and  $C$  for  $B^0 \rightarrow J/\psi K_S^0$  to demonstrate GFlaT's effectiveness in Sec. V and conclude in Sec. VI.

## II. DETECTOR AND SIMULATION

We evaluate GFlaT's performance using a  $(362 \pm 2) \text{ fb}^{-1}$  data set collected with the Belle II detector in 2019–2022. The Belle II detector is located at SuperKEKB, which collides electrons and positrons at and near the  $\Upsilon(4S)$  resonance [25]. It is cylindrical and includes a two-layer silicon-pixel detector (PXD) surrounded by a four-layer double-sided silicon-strip detector [26] and a 56-layer central drift chamber (CDC). These detectors reconstruct trajectories of charged particles (tracks). Only one sixth of the second layer of the PXD was installed for the data analyzed here. The symmetry axis of these detectors,  $z$ , is nearly coincident

with the direction of the electron beam. Surrounding the CDC, which also measures  $dE/dx$  ionization energy-loss, is a time-of-propagation detector [27] in the barrel and an aerogel-based ring-imaging Cherenkov detector in the forward ( $+z$ ) endcap region. These detectors provide information for charged-particle identification. Surrounding them is an electromagnetic calorimeter (ECL) based on CsI(Tl) crystals that primarily measures the energies and times of detection of photons and electrons. Outside it is a superconducting solenoid magnet that provides a 1.5 T field in the  $z$  direction. Its flux return is instrumented with resistive-plate chambers and plastic scintillator modules to detect muons,  $K_L^0$ , and neutrons.

We use simulated data to train GFlaT, estimate reconstruction efficiencies and background contributions, and construct fit models. We generate  $e^+e^- \rightarrow \Upsilon(4S) \rightarrow B\bar{B}$  using EVTGEN [28] and PYTHIA8 [29] and  $e^+e^- \rightarrow q\bar{q}$  with  $q$  indicating a  $u, d, c$ , or  $s$  quark using KKMC [30] and PYTHIA8. We simulate particle decays using EVTGEN interfaced with PYTHIA8, and the interaction of particles with the detector using GEANT4 [31]. Our simulation includes effects of beam-induced backgrounds [32]. Events in both simulation and data are reconstructed using the Belle II analysis software framework [33, 34].

## III. GFLAT

GFlaT is designed to run after  $B_{\text{sig}}$  is reconstructed and uses information from the tracks and energy deposits in the ECL (clusters) not associated with  $B_{\text{sig}}$ , in the same manner as the category-based flavor tagger [14]. We refer to these tracks and clusters as the rest of the event (ROE), which mostly originates from  $B_{\text{tag}}$ . Tracks from the ROE must be within the CDC and have points of closest approach (POCAs) to the  $e^+e^-$  interaction region (IR) that are less than 3 cm from the IR in the  $z$  direction and less than 1 cm from it in the transverse plane. The shape and location of the IR are determined from  $e^+e^- \rightarrow \mu^+\mu^-$  events in 30-minute intervals. We retain only the first 16 charged particles in the ROE, ordered by decreasing momentum in the lab frame. According to simulation, the average number of charged particles in the ROE is 4.8, and less than 0.001% of events have more than 16 charged particles.

GFlaT uses 25 input variables for each ROE charged particle: the lab-frame Cartesian components of its momentum and the displacement of its POCA from the IR; particle-identification likelihoods for each of the six possible charged final-state particles,  $e, \mu, \pi, K$ , proton, and deuteron; and the products of the charge of the particle and the output of the category-based flavor tagger for each of its 13 categories.<sup>3</sup> The input variables have the

<sup>3</sup> corresponding to  $q_{\text{cand}}y_{\text{cat}}$  defined in Ref. [14].

same distributions for  $B^0$  and  $\bar{B}^0$  except for differences in the detection and reconstruction efficiency for negative and positive charged particles.

GFlaT uses a dynamic-graph-convolutional-neural-network that has been used for jet tagging at LHC experiments [35]. GFlaT first processes the input variables using the EdgeConv algorithm [18], which consists of three neural networks: edge and node networks run in parallel, and a weight network runs on their output. In the context of graph-neural-networks, the set of ROE charged particles is a graph with each particle a node and each pair an edge. The node network processes the variables of each particle to update them. The edge network processes the variables of each pair of particles to update the variables of each particle. To reduce computational resources, with no impact on performance, the edge network processes information from pairs formed from only the five nearest neighbors to each particle. The weight network processes the outputs of the edge and node networks with a squeeze-and-excitation algorithm that calculates weights based on variable importance [36]. The output of the EdgeConv consists of the updated variables for each particle that are improved to more accurately reflect the characteristics of each particle.

GFlaT runs EdgeConv twice. The first run processes the measured particle variables, with its edge network finding nearest neighbors based on POCAs. The second run processes the output of the first run, with its edge network finding nearest neighbors based on particle similarity using the updated particle variables. To keep output reasonably symmetric between  $B^0$  and  $\bar{B}^0$ , the output variables of each particle from the second EdgeConv are multiplied by its charge. The averages, maxima, and minima of the outputs are processed with a final network, the event network, which outputs one variable,  $qr_{\text{GFlaT}}$ , which is in  $[-1, 1]$ , with  $q_{\text{tag}} = \text{sign}(qr_{\text{GFlaT}})$  and  $r = |qr_{\text{GFlaT}}|$ .

We train GFlaT using simulated events in which  $B_{\text{tag}}$  decays generically according to known (if known) or assumed (otherwise) branching fractions [37] and  $B_{\text{sig}}$  decays to  $\nu\bar{\nu}$ , so that all reconstructed tracks and ECL clusters form the ROE. The training data set consists of  $5 \times 10^6$  events; the independent validation data set consists of  $8 \times 10^5$  events. We minimize binary cross-entropy loss with the Adam optimizer [38] and train with a one-cycle learning schedule [39]. The learning rate increases linearly from  $5 \times 10^{-4}$  to  $3 \times 10^{-3}$  over five epochs, then decreases linearly to its initial value over five epochs, and finally decreases linearly over ten epochs to  $10^{-6}$ .

Figure 1 shows the  $qr$  distributions for true  $B^0$  and  $\bar{B}^0$  for independent test data consisting of  $1 \times 10^5$  events from GFlaT and the category-based flavor tagger. The latter has more reliable tagging information than reported in Ref. [14], due to recent improvements in particle identification and parameter tuning. GFlaT better distinguishes between  $B^0$  and  $\bar{B}^0$  than the category-based flavor tagger: the peaks at  $|qr| \approx 1$  are higher and the bumps at  $|qr| \approx 0$  and  $|qr| \approx 0.65$  are smaller.

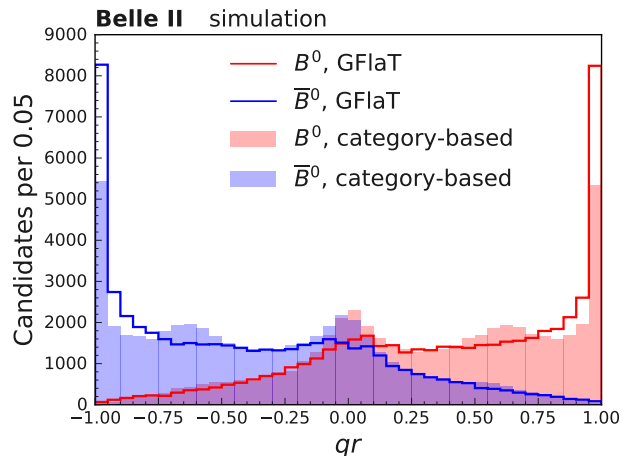


Figure 1. Distributions of  $qr$  for true  $B^0$  and  $\bar{B}^0$  from GFlaT and the category-based flavor tagger in simulated data.

Figure 2 shows the  $qr$  distributions for events classified according to the presence of charged leptons or kaons in the ROE. The ROE contains a charged lepton and a charged kaon in 22.2% of events, a charged lepton and no charged kaon in 22.9%, a charged kaon and no charged lepton in 31.5%, and neither in 23.4%. The distributions indicate that performance is optimal when both a lepton and a kaon are present, with the contribution from leptons being particularly significant. The distributions also reveal that the bump at  $|qr| \approx 0.65$  in the category-based flavor tagger is due to events with charged kaons, which indicates that flavor assignment in such events is less reliable since a  $K^-$ , predominantly associated with  $\bar{B}^0$  decays, can also originate from a  $B^0$  decay, for example through decay to a  $D^-$  with  $D^- \rightarrow \bar{K}^0 K^-$ . Since GFlaT accounts for the relationships between final-state particles, it can better discern the origin of the tracks; and so its output does not peak at  $|qr| \approx 0.65$  for those events, but instead at  $|qr| \approx 1$ . Both flavor taggers perform poorly for events with neither a charged lepton nor a charged kaon, consisting mostly of pions, but GFlaT's output still exhibits a visible improvement. A charged pion from  $B^0$  decay, such as  $B^0 \rightarrow D^- \pi^+$ , or through an intermediate resonance that decays via the strong force, correlates with the  $B$  flavor. The GFlaT algorithm exploits this correlation more effectively to improve performance.

#### IV. CALIBRATION AND PERFORMANCE

We evaluate GFlaT's performance using events in which  $B_{\text{sig}}$  decays to the  $D^{(*)-} \pi^+$  final state. The flavor of  $B_{\text{sig}}$  is determined by the charge of the pion, neglecting the wrong-sign contribution. We fit the  $\Delta t$  probability density model to the background-subtracted  $\Delta t$  distribution, accounting for resolution effects, to determine the

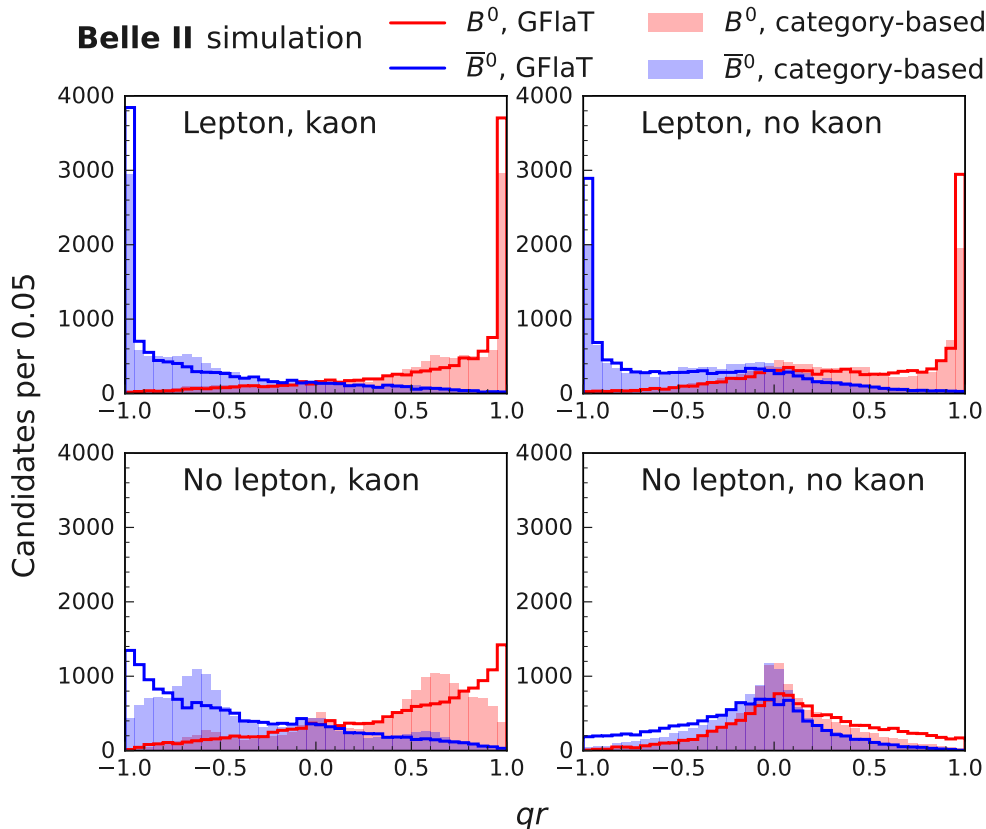


Figure 2. Distributions of  $qr$  for true  $B^0$  and  $\bar{B}^0$  from GFlaT and the category-based flavor tagger for events classified according to the presence of charged leptons or charged kaons in the ROE in simulation data.

wrong-tag probability  $w$  in each  $r$  bin. We subtract the background with  $sWeight$  [40, 41] using the  $B$  energy as a discriminating variable.

We reconstruct  $D^-$  candidates via  $D^- \rightarrow K^+\pi^-\pi^-$  and  $D^{*-}$  via  $D^{*-} \rightarrow \bar{D}^0\pi^-$  with  $\bar{D}^0 \rightarrow K^+\pi^-$ ,  $K^+\pi^-\pi^0$ , or  $K^+\pi^-\pi^+\pi^-$ . Tracks must originate from the IR and have polar angles within the CDC.

We reconstruct  $\pi^0$  candidates via  $\pi^0 \rightarrow \gamma\gamma$ , forming photon candidates from ECL clusters not associated with any tracks. To suppress beam-background photons, we require each cluster have an energy greater than 120 MeV, 30 MeV, or 80 MeV if it is in the forward, barrel, or backward region of the ECL, which corresponds to the lab-frame polar angle ranges  $[12.4, 31.4]^\circ$ ,  $[32.2, 128.7]^\circ$ , and  $[130.7, 155.1]^\circ$ , respectively. The angle between the photon momenta must be less than  $52^\circ$  in the lab frame and the diphoton mass must be in the range  $[121, 142]$  MeV, which is centered on the known  $\pi^0$  mass and is six units of diphoton mass resolution wide.

One of the  $D$ 's decay products must be consistent with being a  $K^+$ , but no particle-identification requirements are placed on the other charged particles. Each  $D^-$  candidate must have a mass in  $[1.860, 1.880]$  GeV, which is centered on the known  $D^-$  mass and is a  $\pm 3\sigma$  range, with  $\sigma$  being the mass resolution. Each  $\bar{D}^0$

candidate reconstructed from  $K^+\pi^-(\pi^+\pi^-)$  must have a mass in  $[1.845, 1.885]$  GeV, which is centered on the known  $\bar{D}^0$  mass and is a  $\pm 5\sigma$  range. Each  $\bar{D}^0$  candidate reconstructed from  $K^+\pi^-\pi^0$  must have a mass in  $[1.810, 1.895]$  GeV, which is an asymmetric range of  $+2.5\sigma$  and  $-4\sigma$  around the known  $\bar{D}^0$  mass to account for energy losses in photon reconstruction.

The  $\pi^-$  from a  $D^{*-}$  candidate decay must have momentum below 300 MeV in the  $e^+e^-$  center-of-mass (c.m.) frame. Each  $D^{*-}$  candidate must have an energy release,  $m(D^{*-}) - m(\bar{D}^0) - m_{\pi^-}$ , in  $[4.6, 7.0]$  MeV, which is centered around the known energy release and six units of its resolution wide.

We reconstruct a  $B^0$  candidate from a  $D^{(*)-}$  candidate and a track that is consistent with being a  $\pi^+$ . For each  $B^0$  candidate, we fit the trajectories and momenta of its decay products according to its decay chain with TREEFIT [42], constraining the  $B^0$  to originate from the IR and the  $D^{(*)}$  to its known mass [37]. We reject  $B^0$  candidates whose fits do not converge. The fraction of rejected signal candidates is 0.4%. We define the signal region from a beam-constrained mass

$$M_{bc} \equiv \sqrt{E_{\text{beam}}^2 - |\vec{p}|^2} \quad (4)$$

and energy difference,  $\Delta E \equiv E - E_{\text{beam}}$ , where  $E_{\text{beam}}$ ,  $E$ , and  $\vec{p}$  are the beam energy and  $B^0$  energy and momentum in the c.m. frame, respectively. The criteria for the signal region are  $M_{\text{bc}} > 5.27$  GeV and  $\Delta E \in [-0.10, 0.25]$  GeV.

We determine the decay position of  $B_{\text{tag}}$  by fitting the trajectories of ROE tracks with RAVE [43]. Unlike TREEFIT, RAVE accounts for the unknown  $B_{\text{tag}}$  decay chain by reducing the impact of a displaced vertex due to potential intermediate  $D$ 's, constraining the  $B_{\text{tag}}$  vertex position to be consistent with the origin and direction of  $B_{\text{sig}}$ . We reject events in which this fit does not converge, which rejects 3.4% of the signal events.

To suppress events not coming from  $e^+e^- \rightarrow B\bar{B}$ , such as  $e^+e^- \rightarrow q\bar{q}$ , we exploit their topological differences, by requiring the ratio of the second to the zeroth Fox-Wolfram moment,  $R_2$ , be less than 0.4 [44]. After applying all selection requirements, the average number of candidates per event is 1.05 and all candidates are retained.

Events passing the above criteria are either correctly identified  $B_{\text{sig}}$  decays or backgrounds from  $B\bar{B}$  and  $q\bar{q}$  events. To separate signal from background, we fit to the  $\Delta E$  distribution using an extended unbinned likelihood, combining data from  $B_{\text{sig}}$  and  $\bar{B}_{\text{sig}}$  and all  $r$  intervals.

We model the signal contribution as the sum of a Gaussian function and a double-sided Crystal-Ball function [45]. Their parameters and their admixture are fixed to values obtained from fitting to simulated data, but a common shift of their peak values and common scaling of their widths are left free to account for differences between data and simulation.

Events in which  $B_{\text{sig}}$  decays to the  $D^{(*)-}K^+$  final state, with the  $K^+$  misidentified as a  $\pi^+$ , peak at  $-50$  MeV in the  $\Delta E$  distribution. According to simulation studies, the fraction of these events to the signal is 2.5%. We model this contribution as a double-sided Crystal Ball function, whose parameters are fixed to values obtained from fitting to simulated data, including the ratio of its yield to the signal, except for the shift of its peak value and the scaling of its width, which are the same as for the signal. Since these events have the same  $\Delta t$  distribution as  $B^0 \rightarrow D^{(*)-}\pi^+$ , we use this contribution as signal in the  $sWeight$  calculation.

We model the  $B\bar{B}$  background contribution as a second-order polynomial, with the ratio of its yield to that of the signal fixed to a value obtained from simulated data. We model the  $q\bar{q}$  background contribution as an exponential function. To constrain the parameters of the  $q\bar{q}$  component, we simultaneously fit to the  $\Delta E$  distribution in a sideband,  $M_{\text{bc}} \in [5.20, 5.24]$  GeV, populated predominantly by  $q\bar{q}$  events. We confirm via simulation studies that the  $\Delta E$  distributions of the  $q\bar{q}$  component in the signal and sideband regions are sufficiently similar to warrant a simultaneous fit.

Figure 3 shows the  $\Delta E$  distributions in the signal region and sideband and the fit results. The fit agrees well with the data. Yields in the signal region are  $77130 \pm 320$  events for the signal (for the sum of the  $D^{(*)-}\pi^+$  and

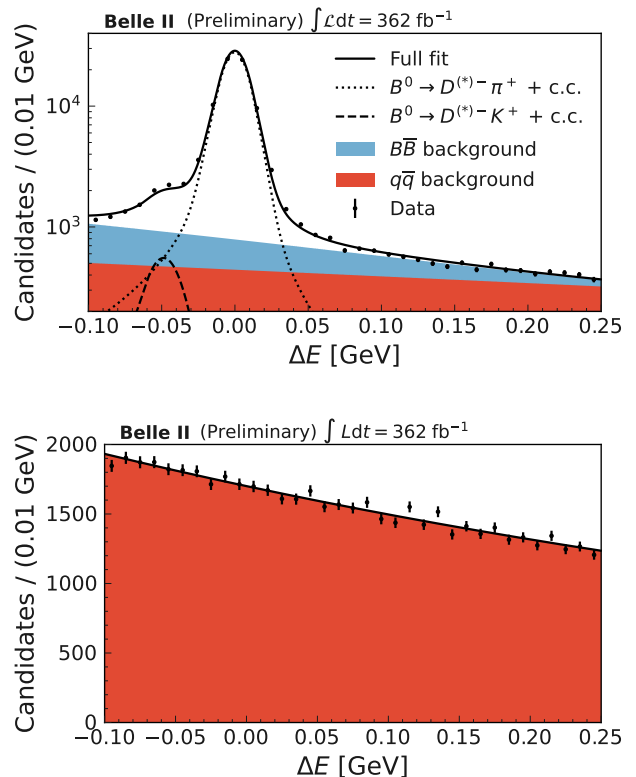


Figure 3. Distributions of  $\Delta E$  for  $B^0 \rightarrow D^{(*)-}\pi^+$  reconstructed in data in the signal region (top) and sideband (bottom) and the best-fit function, with background components stacked.

$D^{(*)-}K^+$  final states),  $8620 \pm 40$  for the  $B\bar{B}$  background, and  $14200 \pm 230$  for the  $q\bar{q}$  background.

We modify equation (2) to account for differences in the wrong-tag probabilities for  $B_{\text{tag}}$  and  $\bar{B}_{\text{tag}}$ , by introducing  $w(B^0) \equiv \bar{w} + \frac{1}{2}\Delta w$  and  $w(\bar{B}^0) \equiv \bar{w} - \frac{1}{2}\Delta w$  and reconstruction efficiency asymmetries for  $B_{\text{sig}}$  and  $\bar{B}_{\text{sig}}$ ,  $a_{\text{sig}}$  and  $a_{\text{tag}}$ , with  $a_x \equiv [\varepsilon(B_x^0) - \varepsilon(\bar{B}_x^0)] / [\varepsilon(\bar{B}_x^0) + \varepsilon(B_x^0)]$ , where  $x$  indicates ‘tag’ or ‘sig’,

$$\begin{aligned}
 P(\Delta t, q_{\text{sig}}, q_{\text{tag}}) = & \\
 & (1 + a_{\text{sig}}q_{\text{sig}}) \frac{e^{-|\Delta t|/\tau}}{4\tau} \left\{ 1 + q_{\text{tag}}[a_{\text{tag}}(1 - 2\bar{w}) - \Delta w] \right. \\
 & \left. + q_{\text{sig}}q_{\text{tag}}(1 - 2\bar{w} + q_{\text{tag}}a_{\text{tag}} - a_{\text{tag}}\Delta w) \cos(\Delta m_d \Delta t) \right\}. \quad (5)
 \end{aligned}$$

We determine  $a_{\text{sig}}$  by fitting the  $\Delta E$  distributions for  $B_{\text{sig}}$  and  $\bar{B}_{\text{sig}}$  separately, using the same model as for their combined fit, without selection criteria on  $B_{\text{tag}}$  to avoid a bias from using  $B_{\text{tag}}$  information. We measure  $a_{\text{sig}} = (-2.53 \pm 0.39)\%$ , which we attribute to charge asymmetries in kaon identification and low-momentum track finding.

We calculate a per-candidate signal probability using  $sWeight$  from the  $\Delta E$ -fit results, allowing us to statisti-

cally subtract background contributions to the  $\Delta t$  distributions. This requires that  $\Delta E$ ,  $\Delta t$ , and  $r$  be independent, which is confirmed in simulation studies.

We calculate  $\Delta t$  from the distance,  $\Delta \ell$ , of the  $B_{\text{sig}}$  vertex from that of  $B_{\text{tag}}$  along the  $\Upsilon(4S)$  boost direction,

$$\Delta t = \frac{\Delta \ell}{\beta \gamma \gamma_B}, \quad (6)$$

where  $\beta \gamma = 0.28$  is the Lorentz boost of the  $\Upsilon(4S)$  in the lab frame and  $\gamma_B = 1.002$  is the Lorentz factor of the  $B$  in the c.m. frame.

To account for resolution and bias in measuring  $\Delta \ell$ , we convolve equation (5) with the resolution function introduced in Ref. [15]. The resolution function consists of a core component modeled by a Gaussian function, a tail component modeled by a weighted sum of a Gaussian and two exponentially modified Gaussian functions, and an outlier component modeled by a Gaussian function. Parameters of the resolution function are shared by all  $r$  bins, except for the highest  $r$  bin. This bin is mostly populated by semileptonic  $B_{\text{tag}}$  decays, which have a better resolution.

We fit simultaneously to the binned background-subtracted  $\Delta t$  distributions in 28 subsets of the data defined by the 7  $r$  intervals, 2 flavors of  $B_{\text{sig}}$ , and 2 flavors of  $B_{\text{tag}}$ . The fit has seven free resolution-function parameters and 21 free flavor-tagger parameters,  $a_{\text{tag}}$ ,  $\bar{w}$ , and  $\Delta w$  in each of the 7  $r$  bins. The uncertainty on the  $\Delta t$  measurement,  $\sigma_{\Delta t}$ , is computed for each event and is a conditional variable in the resolution function. We use a histogram with 500 bins in each data subset as the probability density function for this variable. We fix  $\Delta m_d$  and  $\tau$  to their world average values [37]. Figure 4 shows the  $\Delta t$  distribution in each  $r$  interval and the result of the fit.

Figure 5 shows the  $qr_{\text{GFlaT}}$  distribution in background-subtracted data and correctly reconstructed simulated events normalized to the data signal yield. Figure 6 shows the dilution factors,  $1 - 2w_i$ , for each  $r$  bin  $i$  for both  $B_{\text{tag}}^0$  and  $\bar{B}_{\text{tag}}^0$ . It shows that  $r$  is a good estimator of  $1 - 2w$  for both tag flavors. The effective tagging efficiency is  $\varepsilon_{\text{tag}} = (37.40 \pm 0.43)\%$ , where the uncertainty is statistical only. Table II in Appendix A lists  $a_{\text{tag}}$ ,  $\bar{w}$ , and  $\Delta w$  for each  $r$  bin.

## V. MEASUREMENT OF $\sin 2\phi_1$ IN $B^0 \rightarrow J/\psi K_S^0$

We demonstrate GFlaT by measuring  $S$  and  $C$  in  $B^0 \rightarrow J/\psi K_S^0$  decays. We reconstruct  $J/\psi$  candidates via  $J/\psi \rightarrow e^+e^-$  or  $\mu^+\mu^-$ . The leptons must fulfill the same track requirements as described for the decay products of  $B^0 \rightarrow D^{(*)-}\pi^+$  and be consistent with both being electrons or both being muons. To account for energy loss due to bremsstrahlung, the four-momenta of photons with lab-frame energy in [75, 1000] MeV detected within 50 mrad of the initial direction of an electron are added to

the electron's four-momentum. Each  $J/\psi \rightarrow e^+e^-$  candidate must have a mass in [2.90, 3.14] GeV; each  $J/\psi \rightarrow \mu^+\mu^-$  candidate must have a mass in [3.00, 3.14] GeV. The resolutions at masses above and below the known  $J/\psi$  mass are 8.0 MeV and 9.0 MeV for electron pairs and 6.3 MeV and 8.3 MeV for muon pairs.

We reconstruct  $K_S^0$  candidates via  $K_S^0 \rightarrow \pi^+\pi^-$ . The pions must have polar angles within the CDC. Each  $K_S^0$  candidate must have a mass in the range [0.45, 0.55] GeV, a successful vertex fit, and a decay vertex displaced from the IR by at least five units of the displacement's uncertainty. The reconstructed  $K_S^0$  mass resolution is 2.0 MeV.

We fit the trajectories and momenta of  $B^0$  decay products with TREEFIT, constraining the  $B^0$  to originate from the IR and the  $J/\psi$  to have its known mass [37]. Each  $B^0$  candidate must have  $M_{\text{bc}}$  greater than 5.27 GeV and  $\Delta E$  in  $[-0.10, 0.25]$  GeV. The  $B_{\text{tag}}$  vertex position is determined as described for  $B_{\text{sig}}^0 \rightarrow D^{(*)-}\pi^+$  above. We require  $R_2$  be less than 0.4 to remove  $q\bar{q}$  background. After applying all selection requirements, the average number of candidates per event is 1.01. All candidates are retained for further analysis.

To validate our analysis, we also measure  $S$  and  $C$  for  $B^0 \rightarrow J/\psi K^*(892)^0$ , for which we expect  $S = 0$ , as this decay mode is flavor-specific, and  $C = 0$  as with  $B^0 \rightarrow J/\psi K_S^0$ . Hereafter,  $K^*(892)^0$  is written as  $K^{*0}$ . We reconstruct  $K^{*0}$  candidates via  $K^{*0} \rightarrow K^+\pi^-$ , requiring the positively charged particle be consistent with a  $K^+$  and the negatively charged particle be consistent with a  $\pi^-$ . Each  $K^{*0}$  candidate must have a mass in [0.8, 1.0] GeV, corresponding to approximately four times the  $K^{*0}$  natural width [37]. All selection criteria on  $J/\psi$  and  $B^0$  candidates are the same as for  $B^0 \rightarrow J/\psi K_S^0$ , except that the  $B^0$  must have  $\Delta E$  in a reduced range,  $[-0.10, 0.10]$  GeV, to reject background from  $B^+ \rightarrow J/\psi K^+$  with a  $\pi^-$  from  $B_{\text{tag}}$  reconstructed as part of  $B_{\text{sig}}$ .

We perform extended unbinned likelihood fits to the  $\Delta E$  distributions to determine signal and background yields and shapes that we use to statistically isolate the signal  $\Delta t$  distributions using  $sWeight$ . We model the signal components as double-sided Crystal-Ball functions with tail parameters fixed to values determined from fits to simulated data and peak values and widths freely determined by the fits to data. We model the background components taking into account both  $B\bar{B}$  and  $q\bar{q}$ , as exponential functions, whose parameters are freely determined by the fits to data.

Figure 7 shows the  $\Delta E$  distributions and the fit results. The best-fit results agree well with the data. For  $B^0 \rightarrow J/\psi K_S^0$ , the signal yield is  $6390 \pm 90$  and the background yield is  $570 \pm 40$ . For  $B^0 \rightarrow J/\psi K^{*0}$ , the signal yield is  $12660 \pm 130$  and the background yield is  $1900 \pm 70$ .

We determine  $S$  and  $C$  by performing a simultaneous fit to the background-subtracted  $\Delta t$  distributions in 14 subsets defined by the 7  $r$  intervals and 2 flavors of  $B_{\text{tag}}$ . To take into account detection and tagging asymmetries,

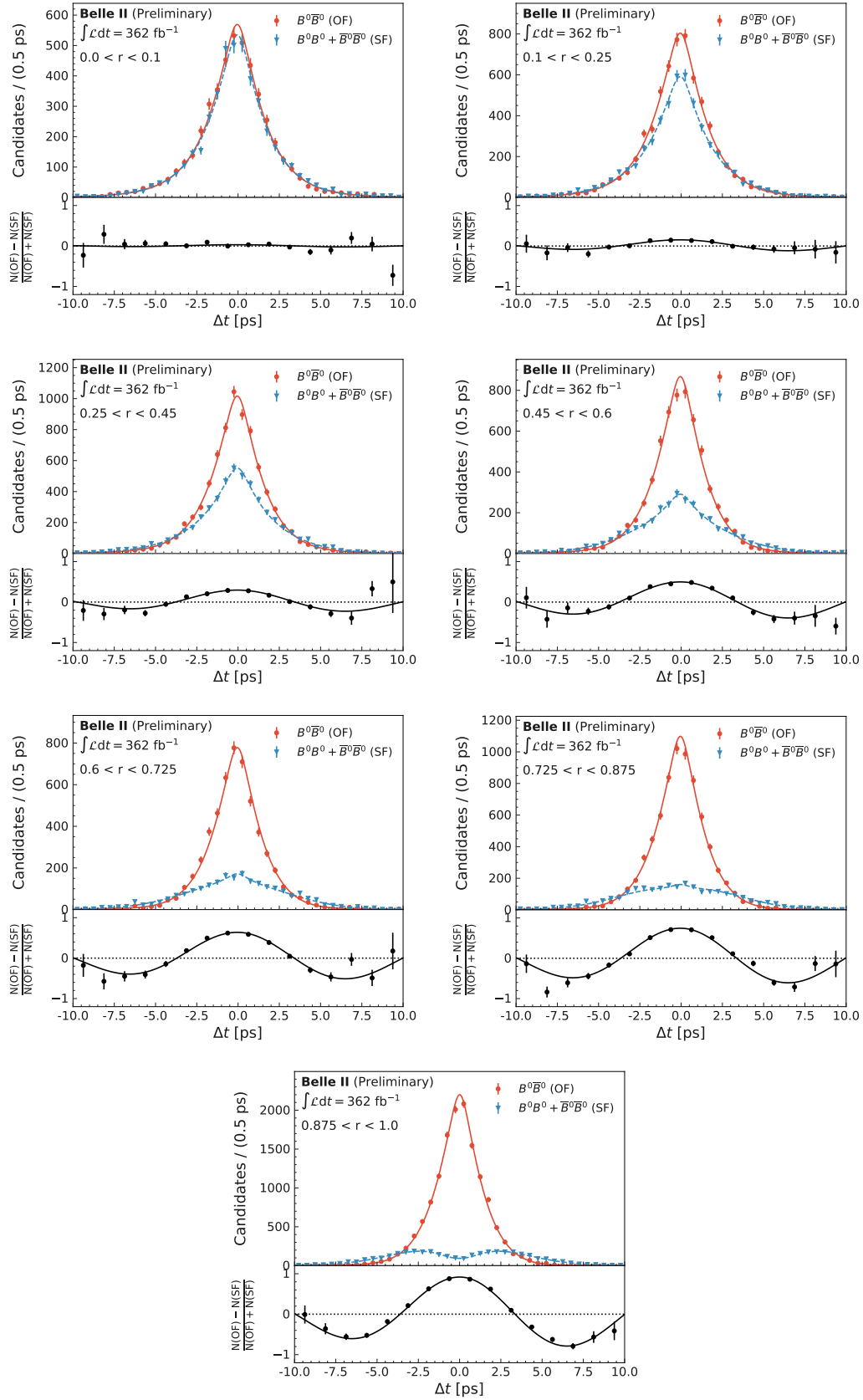


Figure 4. Background-subtracted  $\Delta t$  distributions of  $B^0 \rightarrow D^{(*)-} \pi^+$  reconstructed in data in each of the seven  $r$  intervals (points) and the best-fit functions for opposite- and like-flavor  $B$  pairs with the corresponding asymmetries.



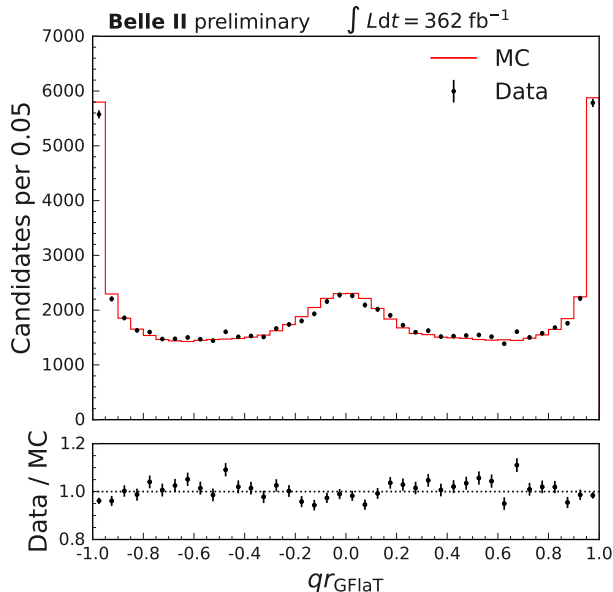


Figure 5. Distributions of  $qr_{\text{GFlaT}}$  for  $B^0 \rightarrow D^{(*)-}\pi^+$  in background-subtracted data and correctly reconstructed simulated events normalized to the data signal yield.

we modify equation (1),

$$P(\Delta t, q_{\text{tag}}) = \frac{e^{-|\Delta t|/\tau}}{4\tau} \left\{ 1 + q_{\text{tag}} [a_{\text{tag}}(1 - 2\bar{w}) - \Delta w] + q_{\text{tag}} (1 - 2\bar{w} + q_{\text{tag}} a_{\text{tag}} - a_{\text{tag}} \Delta w) \times [S \sin(\Delta m_d \Delta t) - C \cos(\Delta m_d \Delta t)] \right\}. \quad (7)$$

To account for resolution and bias in determining  $\Delta t$ , we use the resolution function of the  $B^0 \rightarrow D^{(*)-}\pi^+$  decays without the outlier component, which shows no impact on the results. The  $a_{\text{tag}}$ ,  $\bar{w}$ ,  $\Delta w$ , and resolution-function parameters are fixed to the values determined from the study of  $B^0 \rightarrow D^{(*)-}\pi^+$ , so that the only parameters left free to vary in the  $\Delta t$  fit are  $S$  and  $C$ . Figure 8 shows the background-subtracted  $\Delta t$  distributions (combining all  $r$  intervals) and the result of the fits. For  $B^0 \rightarrow J/\psi K_S^0$ ,  $S = (0.724 \pm 0.035)$  and  $C = (-0.035 \pm 0.026)$ . The statistical correlation between  $S$  and  $C$  is 0.32. For  $B^0 \rightarrow J/\psi K^{*0}$ ,  $S = (-0.018 \pm 0.026)$  and  $C = (0.008 \pm 0.019)$ ; as expected, both are consistent with zero. The uncertainties are statistical only.

Additionally, we fit the  $B^0 \rightarrow J/\psi K_S^0$  candidates without distinguishing between  $B_{\text{tag}}$  and  $\bar{B}_{\text{tag}}$ , therefore removing the ability to observe  $\bar{C}P$  violation, with  $\tau$  free. This checks for potential problems in the modeling of the resolution function, which would likely result in  $\tau$  being biased from its expected value. We measure the  $B^0$  lifetime to be  $(1.514 \pm 0.022)$  ps, which agrees with the

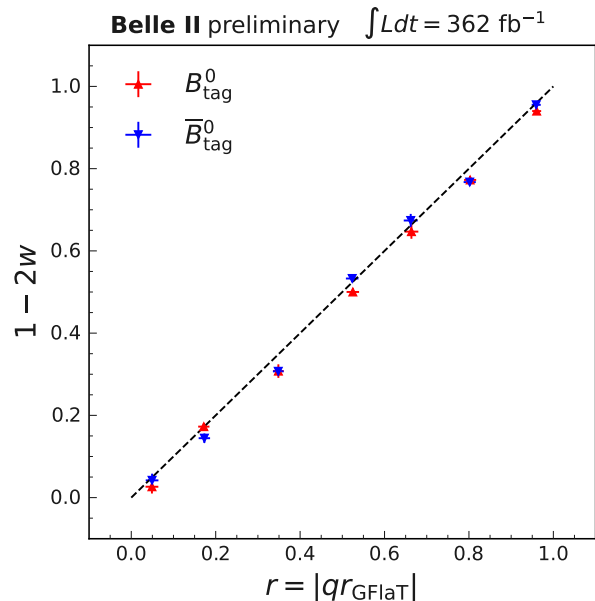


Figure 6. Dilution factors  $1 - 2w$  of  $B^0 \rightarrow D^{(*)-}\pi^+$  as functions of their GFlaT predictions,  $r$  for  $B_{\text{tag}}^0$ ,  $1 - 2\bar{w} - \Delta w$ , and  $\bar{B}_{\text{tag}}^0$ ,  $1 - 2\bar{w} + \Delta w$ ; the dashed line shows  $r = 1 - 2w$ .

current world average [37]. The uncertainty is statistical only.

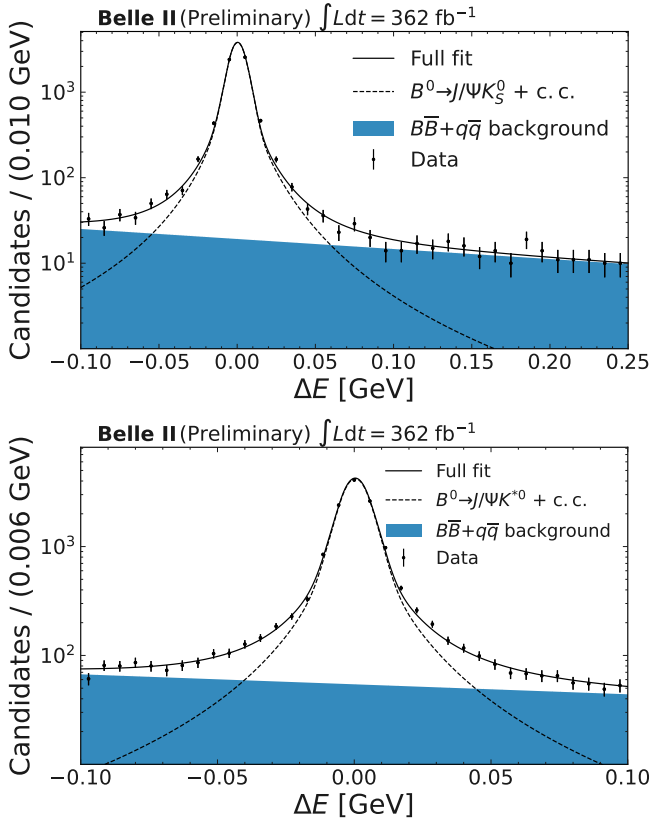
Table I lists the statistical and systematic uncertainties on  $\varepsilon_{\text{tag}}$  for  $B^0 \rightarrow D^{(*)-}\pi^+$  and  $S$  and  $C$  for  $B^0 \rightarrow J/\psi K_S^0$ . Statistical uncertainties are computed by bootstrapping [46], resampling the  $B^0 \rightarrow D^{(*)-}\pi^+$  and  $B^0 \rightarrow J/\psi K_S^0$  data 1000 times each. The statistical uncertainties are larger than the sum in quadrature of all the individual systematic uncertainties.

Uncertainties on the alignment of the tracking system of Belle II detector [47], the shape and location of the IR, and the  $e^+e^-$  beam energy propagate to uncertainties on  $\Delta t$ , resulting in potential changes to  $\varepsilon_{\text{tag}}$ ,  $S$ , and  $C$ . We determine  $\varepsilon_{\text{tag}}$ ,  $S$ , and  $C$  from simulated events reconstructed assuming four detector misalignment scenarios and take their changes, added in quadrature, as systematic uncertainties. Both the IR and beam energy are determined from  $e^+e^- \rightarrow \mu^+\mu^-$  events in 30-minute intervals. We determine  $\varepsilon_{\text{tag}}$ ,  $S$ , and  $C$  with the parameters of the IR and beam energy varied by their uncertainties and take the shifts as systematic uncertainties.

Uncertainties on  $\Delta E$ -fit component shapes propagate to uncertainties on the background-subtracted  $\Delta t$  distributions, resulting in potential changes to  $\varepsilon_{\text{tag}}$ ,  $S$ , and  $C$ . We fit using various models and take any resulting shifts, added in quadrature, as systematic uncertainties. For the fit to  $B^0 \rightarrow D^{(*)-}\pi^+$  data, these models are inclusion of an additional Gaussian function to model a small peaking background from  $B\bar{B}$  events, variation of the fixed ratio of  $B\bar{B}$  events to  $B^0 \rightarrow D^{(*)-}\pi^+$  events by  $\pm 20\%$ , and the

Table I. Systematic and statistical uncertainties on  $\varepsilon_{\text{tag}}$  for  $B^0 \rightarrow D^{(*)-} \pi^+$  and,  $S$  and  $C$  for  $B^0 \rightarrow J/\psi K_S^0$ .

Source	$\varepsilon_{\text{tag}}$ [%]	$S$	$C$
Detector alignment	0.08	0.005	0.003
Interaction region	0.16	0.002	0.002
Beam energy	0.03	< 0.001	0.001
$\Delta E$ -fit background model	0.11	0.001	0.001
$\Delta E$ -fit signal model	0.08	0.003	0.006
$sWeight$ background subtraction	0.24	0.001	0.001
Fixed resolution-function parameters	0.07	0.004	0.004
$\tau$ and $\Delta m_d$	0.06	0.001	< 0.001
$\sigma_{\Delta t}$ binning	0.04	< 0.001	< 0.001
$\Delta t$ -fit bias	0.09	0.002	0.005
$CP$ violation in $B_{\text{tag}}$ decay		0.011	0.006
$B^0 \rightarrow D^{(*)-} \pi^+$ sample size		0.004	0.007
Total systematic uncertainty	0.36	0.014	0.013
Statistical uncertainty	0.43	0.035	0.026

Figure 7. Distributions of  $\Delta E$  for  $B^0 \rightarrow J/\psi K_S^0$  (top) and  $B^0 \rightarrow J/\psi K^{*0}$  (bottom) and the best-fit functions.

freeing of the ratio of  $B^0 \rightarrow D^{(*)-} K^+$  to  $B^0 \rightarrow D^{(*)-} \pi^+$  events. Variations to the background models in the fits to  $B^0 \rightarrow J/\psi K_S^0$  data have negligible impact. For the signal components, we varied fixed parameters within their uncertainties one by one.

The process of subtracting the backgrounds using  $sWeight$  is itself a source of uncertainty. For  $B^0 \rightarrow$

$J/\psi K_S^0$ , it is accounted for in the  $\Delta t$ -fit bias discussed below. We account for the uncertainty in the background subtraction in  $B^0 \rightarrow D^{(*)-} \pi^+$  by determining  $\varepsilon_{\text{tag}}$ ,  $S$ , and  $C$  replacing the  $\Delta t$  distributions with those from  $1 \text{ ab}^{-1}$  of simulated  $B^0 \rightarrow D^{(*)-} \pi^+$  data that either contain signal events or signal and background events with background subtraction using  $sWeight$ , and take the differences as systematic uncertainties. This is the dominant systematic uncertainty on  $\varepsilon_{\text{tag}}$ .

Uncertainties on  $\Delta t$ -fit shape parameters directly propagate to changes to  $\varepsilon_{\text{tag}}$ ,  $S$ , and  $C$ . We repeat the fits with fixed resolution-function parameters freed one at a time and take the resulting changes to  $\varepsilon_{\text{tag}}$ ,  $S$ , and  $C$ , added in quadrature, as systematic uncertainties. We also repeat the fits with  $\tau$  and  $\Delta m_d$  varied within their known uncertainties [37] and take the resulting changes, added in quadrature, as systematic uncertainties. Finally, we repeat the fits with the numbers of bins for the  $\sigma_{\Delta t}$  histogrammed probability density functions varied between 200 and 1000 and take the largest changes as systematic uncertainties.

The  $\Delta t$  fits have biases that we determine from fits to simulated data sets equivalent in size to the real data, 20 such sets for  $B^0 \rightarrow D^{(*)-} \pi^+$  and 290 for  $B^0 \rightarrow J/\psi K_S^0$ . We take the quadratic sum of the biases and their uncertainties as systematic uncertainties.

Equation (7) does not account for  $CP$  violation in  $B_{\text{tag}}$  decays [48]. This yields a systematic uncertainty determined in Ref. [3], which is the dominant systematic uncertainty on  $S$ . We propagate the statistical uncertainties on GFLaT's parameters and resolution-function parameters, arising from the  $B^0 \rightarrow D^{(*)-} \pi^+$  sample size, to uncertainties on  $S$  and  $C$  by repeating the fits for each  $B^0 \rightarrow D^{(*)-} \pi^+$  bootstrap sample.

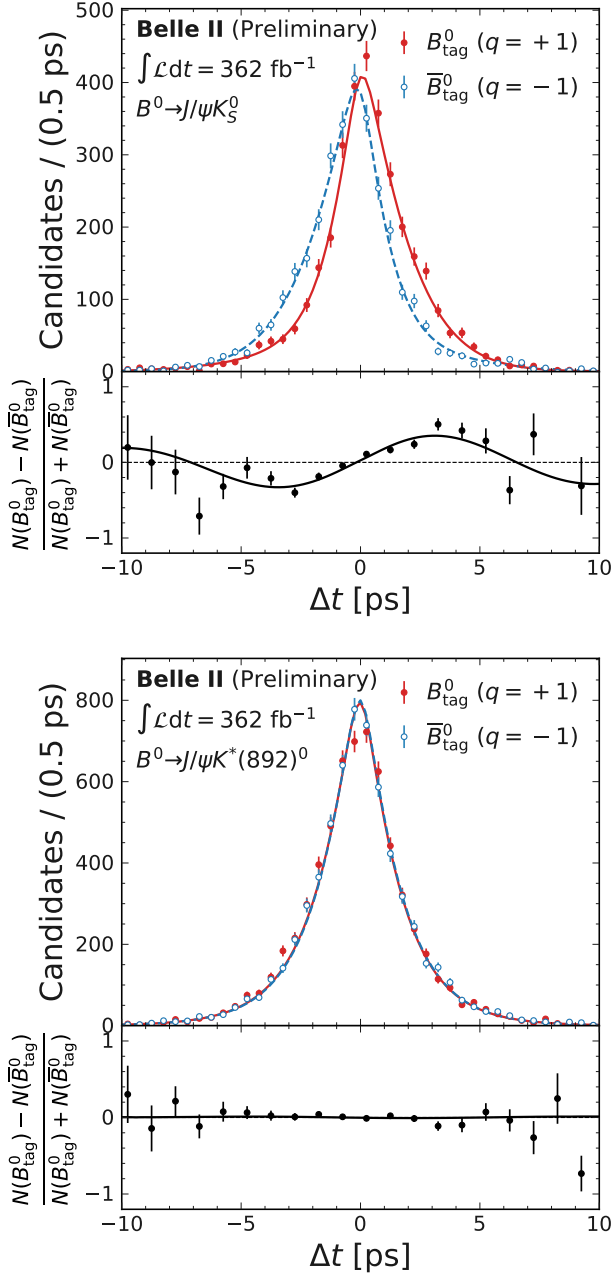


Figure 8. Background-subtracted  $\Delta t$  distributions for  $B^0 \rightarrow J/\psi K_S^0$  (top) and  $B^0 \rightarrow J/\psi K^{*0}$  (bottom) in the full  $r$  range (points) and the best-fit function (lines) for opposite- and like-flavor  $B$  pairs and the corresponding asymmetries.

## VI. SUMMARY

We report on a new  $B$  flavor tagger, GFlaT, for Belle II that uses a graph-neural-network to account for the correlated information among the decay products of the tag-side  $B$ . We calibrate it using flavor-specific hadronic  $B$  decays reconstructed in a  $(362 \pm 2) \text{ fb}^{-1}$  sample of Belle II

data and determine an effective tagging efficiency of

$$\varepsilon_{\text{tag}} = (37.40 \pm 0.43 \pm 0.36)\%, \quad (8)$$

where the first uncertainty is statistical and the second is systematic. For comparison, using the same data, we determine  $\varepsilon_{\text{tag}} = (31.68 \pm 0.45)\%$  for the Belle II category-based flavor tagger.<sup>4</sup> The GFlaT algorithm thus has an 18% better effective tagging efficiency.

We demonstrate GFlaT by measuring  $S$  and  $C$  for  $B^0 \rightarrow J/\psi K_S^0$ ,

$$S = 0.724 \pm 0.035 \pm 0.014, \quad (9)$$

$$C = -0.035 \pm 0.026 \pm 0.013, \quad (10)$$

with a statistical correlation between  $S$  and  $C$  of 0.32, which agree with previous measurements [2–4, 37]. The statistical uncertainties are 8% and 7% smaller, respectively, than they would be if measured using the category-based flavor tagger, as expected given GFlaT’s higher effective tagging efficiency. From  $S$ , we calculate  $\phi_1 = (23.2 \pm 1.5 \pm 0.6)^\circ$ .<sup>5</sup>

## ACKNOWLEDGEMENTS

This work, based on data collected using the Belle II detector, which was built and commissioned prior to March 2019, was supported by Higher Education and Science Committee of the Republic of Armenia Grant No. 23LCG-1C011; Australian Research Council and Research Grants No. DP200101792, No. DP210101900, No. DP210102831, No. DE220100462, No. LE210100098, and No. LE230100085; Austrian Federal Ministry of Education, Science and Research, Austrian Science Fund No. P 31361-N36 and No. J4625-N, and Horizon 2020 ERC Starting Grant No. 947006 “InterLeptons”; Natural Sciences and Engineering Research Council of Canada, Compute Canada and CANARIE; National Key R&D Program of China under Contract No. 2022YFA1601903, National Natural Science Foundation of China and Research Grants No. 11575017, No. 11761141009, No. 11705209, No. 11975076, No. 12135005, No. 12150004, No. 12161141008, and No. 12175041, and Shandong Provincial Natural Science Foundation Project ZR2022JQ02; the Czech Science Foundation Grant No. 22-18469S; European Research Council, Seventh Framework PIEF-GA-2013-622527, Horizon 2020 ERC-Advanced Grants No. 267104 and No. 884719, Horizon 2020 ERC-Consolidator

<sup>4</sup> Systematic uncertainties were not explicitly computed for the category-based flavor tagger, as they are expected to be very similar to and fully correlated with those from GFlaT.

<sup>5</sup> The other solution  $\pi/2 - \phi_1$  is excluded from independent measurements [49]

Grant No. 819127, Horizon 2020 Marie Skłodowska-Curie Grant Agreement No. 700525 “NIOBE” and No. 101026516, and Horizon 2020 Marie Skłodowska-Curie RISE project JENNIFER2 Grant Agreement No. 822070 (European grants); L’Institut National de Physique Nucléaire et de Physique des Particules (IN2P3) du CNRS and L’Agence Nationale de la Recherche (ANR) under grant ANR-21-CE31-0009 (France); BMBF, DFG, HGF, MPG, and AvH Foundation (Germany); Department of Atomic Energy under Project Identification No. RTI 4002, Department of Science and Technology, and UPES SEED funding programs No. UPES/R&D-SEED-INFRA/17052023/01 and No. UPES/R&D-SOE/20062022/06 (India); Israel Science Foundation Grant No. 2476/17, U.S.-Israel Binational Science Foundation Grant No. 2016113, and Israel Ministry of Science Grant No. 3-16543; Istituto Nazionale di Fisica Nucleare and the Research Grants BELLE2; Japan Society for the Promotion of Science, Grant-in-Aid for Scientific Research Grants No. 16H03968, No. 16H03993, No. 16H06492, No. 16K05323, No. 17H01133, No. 17H05405, No. 18K03621, No. 18H03710, No. 18H05226, No. 19H00682, No. 20H05850, No. 20H05858, No. 22H00144, No. 22K14056, No. 22K21347, No. 23H05433, No. 26220706, and No. 26400255, the National Institute of Informatics, and Science Information NETwork 5 (SINET5), and the Ministry of Education, Culture, Sports, Science, and Technology (MEXT) of Japan; National Research Foundation (NRF) of Korea Grants No. 2016R1D1A1B02012900, No. 2018R1A2B3003643, No. 2018R1A6A1A06024970, No. 2019R1I1A3A01058933, No. 2021R1A6A1A-03043957, No. 2021R1F1A1060423, No. 2021R1F1A-1064008, No. 2022R1A2C1003993, and No. RS-2022-00197659, Radiation Science Research Institute, Foreign Large-Size Research Facility Application Supporting project, the Global Science Experimental Data Hub Center of the Korea Institute of Science and Technology Information and KREONET/GLORIAD; Universiti Malaya RU grant, Akademi Sains Malaysia, and Ministry of Education Malaysia; Frontiers of Science Program Contracts No. FOINS-296, No. CB-221329, No. CB-236394, No. CB-254409, and No. CB-180023, and SEP-CINVESTAV Research Grant No. 237 (Mexico); the Polish Ministry of Science and Higher Education and the National Science Center; the Ministry of Science and Higher Education of the Russian Federation and the HSE University Basic Research Program, Moscow; University of Tabuk Research Grants No. S-0256-1438 and No. S-0280-1439 (Saudi Arabia); Slovenian Research Agency and Research Grants No. J1-9124 and No. P1-0135; Agencia Estatal de Investigacion, Spain Grant No. RYC2020-029875-I and Generalitat Valenciana, Spain Grant No. CIDEGENT/2018/020; National Science and Technology Council, and Ministry of Education (Taiwan); Thailand Center of Excellence in Physics; TUBITAK ULAKBIM (Turkey); National Research

Foundation of Ukraine, Project No. 2020.02/0257, and Ministry of Education and Science of Ukraine; the U.S. National Science Foundation and Research Grants No. PHY-1913789 and No. PHY-2111604, and the U.S. Department of Energy and Research Awards No. DE-AC06-76RLO1830, No. DE-SC0007983, No. DE-SC0009824, No. DE-SC0009973, No. DE-SC0010007, No. DE-SC0010073, No. DE-SC0010118, No. DE-SC0010504, No. DE-SC0011784, No. DE-SC0012704, No. DE-SC0019230, No. DE-SC0021274, No. DE-SC0021616, No. DE-SC0022350, No. DE-SC0023470; and the Vietnam Academy of Science and Technology (VAST) under Grants No. NVCC.05.12/22-23 and No. DL0000.02/24-25.

These acknowledgements are not to be interpreted as an endorsement of any statement made by any of our institutes, funding agencies, governments, or their representatives.

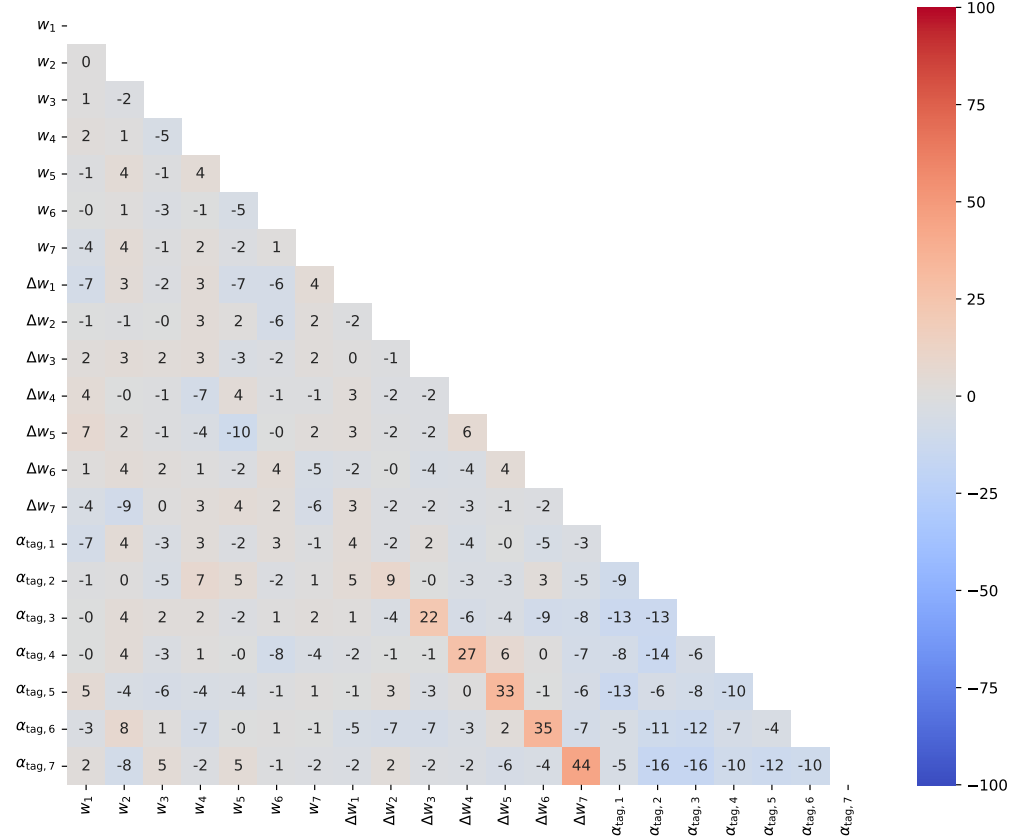
We thank the SuperKEKB team for delivering high-luminosity collisions; the KEK cryogenics group for the efficient operation of the detector solenoid magnet; the KEK computer group and the NII for on-site computing support and SINET6 network support; and the raw-data centers at BNL, DESY, GridKa, IN2P3, INFN, and the University of Victoria for off-site computing support.

## Appendix A: GF<sub>1A</sub>T parameters

Table II lists  $a_{\text{tag}}$ ,  $\bar{w}$ , and  $\Delta w$  for each  $r$  bin, measured from events with  $B^0 \rightarrow D^{(*)-}\pi^+$ . The sources of systematic uncertainty are the same as listed in Table I for  $\varepsilon_{\text{tag}}$ . Figure 9 shows the statistical correlation coefficients between the parameters that are used as inputs to estimate systematic uncertainties for  $S$  and  $C$ .

Table II. GFLaT parameters in each  $r$  bin.

$r$ bin	$a_{\text{tag}} [\%]$	$\bar{w} [\%]$	$\Delta w [\%]$
[0.0, 0.1]	$-1.72 \pm 1.47 \pm 1.32$	$48.29 \pm 0.78 \pm 0.75$	$0.78 \pm 1.16 \pm 0.71$
[0.1, 0.25]	$-0.94 \pm 1.36 \pm 1.45$	$42.07 \pm 0.72 \pm 0.32$	$-1.41 \pm 1.06 \pm 0.92$
[0.25, 0.45]	$-0.28 \pm 1.28 \pm 1.46$	$34.63 \pm 0.61 \pm 0.61$	$-0.04 \pm 0.97 \pm 1.28$
[0.45, 0.6]	$3.21 \pm 1.44 \pm 1.50$	$24.17 \pm 0.68 \pm 0.36$	$1.64 \pm 1.13 \pm 0.52$
[0.6, 0.725]	$1.17 \pm 1.58 \pm 1.47$	$16.98 \pm 0.68 \pm 0.92$	$1.36 \pm 1.15 \pm 0.72$
[0.725, 0.875]	$-1.13 \pm 1.30 \pm 1.55$	$11.50 \pm 0.53 \pm 0.39$	$-0.26 \pm 0.92 \pm 0.71$
[0.875, 1.0]	$-0.18 \pm 0.91 \pm 1.30$	$2.62 \pm 0.27 \pm 0.14$	$0.75 \pm 0.53 \pm 0.60$

Figure 9. Correlation coefficients, in  $10^{-2}$ , between the GFLaT parameters. Subscripts indicate  $r$  bins.

- [1] M. Kobayashi and T. Maskawa, *CP* violation in the renormalizable theory of weak interaction, *Prog. Theor. Phys.* **49**, 652 (1973).
- [2] B. Aubert *et al.* (BaBar collaboration), Measurement of Time-Dependent *CP* Asymmetry in  $B^0 \rightarrow c\bar{c}K^{(*)0}$  Decays, *Phys. Rev. D* **79**, 072009 (2009), arXiv:0902.1708 [hep-ex].
- [3] I. Adachi *et al.* (Belle collaboration), Precise measurement of the *CP* violation parameter  $\sin 2\phi_1$  in  $B^0 \rightarrow (c\bar{c})K^0$  decays, *Phys. Rev. Lett.* **108**, 171802 (2012), arXiv:1201.4643 [hep-ex].
- [4] R. Aaij *et al.* (LHCb collaboration), Measurement of *CP* violation in  $B^0 \rightarrow \psi(\rightarrow \ell^+\ell^-)K_S^0(\rightarrow \pi^+\pi^-)$  decays, *Phys. Rev. Lett.* **132**, 021801 (2024), arXiv:2309.09728 [hep-ex].
- [5] J. P. Lees *et al.* (BaBar collaboration), Measurement of *CP* Asymmetries and Branching Fractions in Charmless Two-Body *B*-Meson Decays to Pions and Kaons, *Phys. Rev. D* **87**, 052009 (2013), arXiv:1206.3525 [hep-ex].
- [6] I. Adachi *et al.* (Belle collaboration), Measurement of the *CP* violation parameters in  $B^0 \rightarrow \pi^+\pi^-$  decays, *Phys. Rev. D* **88**, 092003 (2013), arXiv:1302.0551 [hep-ex].
- [7] R. Aaij *et al.* (LHCb collaboration), Observation of *CP* violation in two-body  $B_{(s)}^0$ -meson decays to charged pions and kaons, *JHEP* **03**, 075, arXiv:2012.05319 [hep-ex].

- [8] B. Aubert *et al.* (BaBar collaboration), A Study of  $B^0 \rightarrow \rho^+ \rho^-$  Decays and Constraints on the CKM Angle  $\alpha$ , *Phys. Rev. D* **76**, 052007 (2007), arXiv:0705.2157 [hep-ex].
- [9] P. Vanhoefer *et al.* (Belle collaboration), Study of  $B^0 \rightarrow \rho^+ \rho^-$  decays and implications for the CKM angle  $\phi_2$ , *Phys. Rev. D* **93**, 032010 (2016), [Addendum: *Phys.Rev.D* 94, 099903 (2016)], arXiv:1510.01245 [hep-ex].
- [10] B. Aubert *et al.* (BaBar collaboration), Measurement of the Branching Fraction, Polarization, and CP Asymmetries in  $B^0 \rightarrow \rho^0 \rho^0$  Decay, and Implications for the CKM Angle  $\alpha$ , *Phys. Rev. D* **78**, 071104 (2008), arXiv:0807.4977 [hep-ex].
- [11] I. I. Y. Bigi and A. I. Sanda, Notes on the Observability of CP Violations in B Decays, *Nucl. Phys. B* **193**, 85 (1981).
- [12] P. Oddone, Detector considerations, *UCLA Linear-Collider BB Factory Concep. Design: Proceedings*, eConf **C870126**, 423 (1987).
- [13] T. Abe *et al.* (Belle II collaboration), Belle II technical design report, arXiv:1011.0352 [physics.ins-det] (2010).
- [14] F. Abudinén *et al.* (Belle II collaboration), B-flavor tagging at Belle II, *Eur. Phys. J. C* **82**, 283 (2022), arXiv:2110.00790 [hep-ex].
- [15] F. Abudinén *et al.* (Belle II collaboration), Measurement of the  $B^0$  lifetime and flavor-oscillation frequency using hadronic decays reconstructed in 2019–2021 Belle II data, *Phys. Rev. D* **107**, L091102 (2023), arXiv:2302.12791 [hep-ex].
- [16] I. Adachi *et al.* (Belle II collaboration), Measurement of decay-time-dependent CP violation in  $B^0 \rightarrow J/\psi K_S^0$  decays using 2019-2021 Belle II data, arXiv:2302.12898 [hep-ex] (2023).
- [17] H. Kakuno *et al.* (Belle collaboration), Neutral B flavor tagging for the measurement of mixing induced CP violation at Belle, *Nucl. Instrum. Meth. A* **533**, 516 (2004), arXiv:hep-ex/0403022.
- [18] Y. Wang, Y. Sun, Z. Liu, S. E. Sarma, M. M. Bronstein, and J. M. Solomon, Dynamic graph cnn for learning on point clouds, *ACM Trans. Graph.* **38**, 10.1145/3326362 (2019).
- [19] K. De Bruyn and R. Fleischer, A Roadmap to Control Penguin Effects in  $B_d^0 \rightarrow J/\psi K_S^0$  and  $B_s^0 \rightarrow J/\psi \phi$ , *JHEP* **03**, 145, arXiv:1412.6834 [hep-ph].
- [20] M. Z. Barel, K. De Bruyn, R. Fleischer, and E. Malami, In pursuit of new physics with  $B_d^0 \rightarrow J/\psi K^0$  and  $B_s^0 \rightarrow J/\psi \phi$  decays at the high-precision Frontier, *J. Phys. G* **48**, 065002 (2021), arXiv:2010.14423 [hep-ph].
- [21] M. Z. Barel, K. De Bruyn, R. Fleischer, and E. Malami, Penguin Effects in  $B_d^0 \rightarrow J/\psi K_S^0$  and  $B_s^0 \rightarrow J/\psi \phi$ , *PoS CKM2021*, 111 (2023), arXiv:2203.14652 [hep-ph].
- [22] I. Dunietz, Clean CKM information from  $B_d(t) \rightarrow D^{*\mp} \pi^\pm$ , *Phys. Lett. B* **427**, 179 (1998), arXiv:hep-ph/9712401.
- [23] A. Das *et al.* (Belle collaboration), Measurements of Branching Fractions for  $B^0 \rightarrow D_s^+ \pi^-$  and  $\bar{B}^0 \rightarrow D_s^+ K^-$ , *Phys. Rev. D* **82**, 051103 (2010), arXiv:1007.4619 [hep-ex].
- [24] B. Aubert *et al.* (BaBar collaboration), Measurement of the Branching Fractions of the Rare Decays  $B^0 \rightarrow D_s^{(*)+} \pi^-$ ,  $B^0 \rightarrow D_s^{(*)+} \rho^-$ , and  $B^0 \rightarrow D_s^{(*)-} K^{(*)+}$ , *Phys. Rev. D* **78**, 032005 (2008), arXiv:0803.4296 [hep-ex].
- [25] K. Akai, K. Furukawa, and H. Koiso, SuperKEKB collider, *Nucl. Instrum. Meth.* **A907**, 188 (2018), arXiv:1809.01958 [physics.acc-ph].
- [26] K. Adamczyk *et al.* (Belle II SVD collaboration), The design, construction, operation and performance of the Belle II silicon vertex detector, *JINST* **17** (11), P11042, arXiv:2201.09824 [physics.ins-det].
- [27] D. Kotchetkov *et al.*, Front-end electronic readout system for the Belle II imaging Time-Of-Propagation detector, *Nucl. Instrum. Meth. A* **941**, 162342 (2019), arXiv:1804.10782 [physics.ins-det].
- [28] D. J. Lange, The EvtGen particle decay simulation package, *Proceedings, 7th International Conference on B physics at hadron machines (BEAUTY 2000): Maagan, Israel, September 13-18, 2000*, *Nucl. Instrum. Meth.* **A462**, 152 (2001).
- [29] T. Sjöstrand, S. Ask, J. R. Christiansen, R. Corke, N. Desai, P. Ilten, S. Mrenna, S. Prestel, C. O. Rasmussen, and P. Z. Skands, An Introduction to PYTHIA 8.2, *Comput. Phys. Commun.* **191**, 159 (2015), arXiv:1410.3012 [hep-ph].
- [30] S. Jadach, B. F. L. Ward, and Z. Wąs, The precision Monte Carlo event generator KK for two-fermion final states in  $e^+e^-$  collisions, *Comput. Phys. Commun.* **130**, 260 (2000), arXiv:hep-ph/9912214 [hep-ph].
- [31] S. Agostinelli *et al.* (GEANT4 collaboration), GEANT4: A simulation toolkit, *Nucl. Instrum. Meth.* **A506**, 250 (2003).
- [32] P. M. Lewis *et al.*, First Measurements of Beam Backgrounds at SuperKEKB, *Nucl. Instrum. Meth. A* **914**, 69 (2019), arXiv:1802.01366 [physics.ins-det].
- [33] T. Kuhr, C. Pulvermacher, M. Ritter, T. Hauth, and N. Braun (Belle II Framework Software Group), The Belle II Core Software, *Comput. Softw. Big Sci.* **3**, 1 (2019), arXiv:1809.04299 [physics.comp-ph].
- [34] Belle II collaboration, Belle II Analysis Software Framework (basf2), <https://doi.org/10.5281/zenodo.5574115>.
- [35] H. Qu and L. Gouskos, ParticleNet: Jet Tagging via Particle Clouds, *Phys. Rev. D* **101**, 056019 (2020), arXiv:1902.08570 [hep-ph].
- [36] J. Hu, L. Shen, and G. Sun, Squeeze-and-excitation networks, *CoRR* **abs/1709.01507** (2017), 1709.01507.
- [37] R. L. Workman *et al.* (Particle Data Group), Review of Particle Physics, *PTEP* **2022**, 083C01 (2022).
- [38] D. P. Kingma and J. Ba, Adam: A method for stochastic optimization, arXiv:1412.6980 [cs.LG] (2017).
- [39] L. N. Smith, A disciplined approach to neural network hyper-parameters: Part 1 – learning rate, batch size, momentum, and weight decay, arXiv e-prints , arXiv:1803.09820 (2018), arXiv:1803.09820 [cs.LG].
- [40] M. Pivk and F. R. Le Diberder, sPlot: A statistical tool to unfold data distributions, *Nucl. Instrum. Meth.* **A555**, 356 (2005), arXiv:physics/0402083 [physics.data-an].
- [41] H. Dembinski, M. Kenzie, C. Langenbruch, and M. Schmelling, Custom Orthogonal Weight functions (COWs) for event classification, *Nucl. Instrum. Meth. A* **1040**, 167270 (2022), arXiv:2112.04574 [stat.ME].
- [42] J.-F. Krohn *et al.* (Belle II Analysis Software Group), Global decay chain vertex fitting at Belle II, *Nucl. Instrum. Meth.* **A976**, 164269 (2020), arXiv:1901.11198 [hep-ex].

- [43] W. Waltenberger, W. Mitaroff, F. Moser, B. Pflugfelder, and H. V. Riedel, The RAVE/VERTIGO vertex reconstruction toolkit and framework, *J. Phys. Conf. Ser.* **119**, 032037 (2008).
- [44] G. C. Fox and S. Wolfram, Observables for the Analysis of Event Shapes in  $e^+e^-$  Annihilation and Other Processes, *Phys. Rev. Lett.* **41**, 1581 (1978).
- [45] T. Skwarnicki, *A study of the radiative CASCADE transitions between the Upsilon-Prime and Upsilon resonances*, Ph.D. thesis, Cracow, INP (1986).
- [46] B. Efron, Bootstrap Methods: Another Look at the Jackknife, *Annals Statist.* **7**, 1 (1979).
- [47] T. Bilka *et al.*, Alignment for the first precision measurements at Belle II, *EPJ Web Conf.* **245**, 02023 (2020).
- [48] O. Long, M. Baak, R. N. Cahn, and D. P. Kirkby, Impact of tag side interference on time dependent  $CP$  asymmetry measurements using coherent  $B^0\bar{B}^0$  pairs, *Phys. Rev. D* **68**, 034010 (2003), arXiv:hep-ex/0303030.
- [49] A. Abdesselam *et al.* (BaBar, Belle), First Observation of CP Violation in  $\bar{B}^0 \rightarrow D_{CP}^{(*)}h^0$  Decays by a Combined Time-Dependent Analysis of BABAR and Belle Data, *Phys. Rev. Lett.* **115**, 121604 (2015), arXiv:1505.04147 [hep-ex].